

Radioactive Planet Formation

Fred C. Adams^{1,2}

¹*Physics Department, University of Michigan, Ann Arbor, MI 48109*

²*Astronomy Department, University of Michigan, Ann Arbor, MI 48109*

ABSTRACT

Young stellar objects are observed to have large X-ray fluxes and are thought to produce commensurate luminosities in energetic particles (cosmic rays). This particle radiation, in turn, can synthesize short-lived radioactive nuclei through spallation. With a focus on ^{26}Al , this paper estimates the expected abundances of radioactive nuclei produced by spallation during the epoch of planet formation. In this model, cosmic rays are accelerated near the inner truncation radii of circumstellar disks, $r_X \approx 0.1$ AU, where intense magnetic activity takes place. For planets forming in this region, radioactive abundances can be enhanced over the values inferred for the early solar system (from meteoritic measurements) by factors of $\sim 10 - 20$. These short-lived radioactive nuclei influence the process of planet formation and the properties of planets in several ways. The minimum size required for planetesimals to become fully molten decreases with increasing levels of radioactive enrichment, and such melting leads to loss of volatile components including water. Planets produced with an enhanced radioactive inventory have significant internal luminosity which can be comparable to that provided by the host star; this additional heating affects both atmospheric mass loss and chemical composition. Finally, the habitable zone of red dwarf stars is coincident with the magnetic reconnection region, so that planets forming at those locations will experience maximum exposure to particle radiation, and subsequent depletion of volatiles.

UAT Concepts: Exoplanet formation (492); Exoplanet astronomy (486)

1. Introduction

The collection of observed planets orbiting other stars shows enormous diversity, which poses a fundamental problem for understanding the process of planet formation. One component of the explanation is that planets are likely to form with a variety of background

conditions, which are provided by the circumstellar disks that give rise to these companions. This paper explores one aspect of the problem by considering the range of possible abundances of short-lived radionuclides (SLRs) that are present during the formation and early evolution of planetary bodies. More specifically, we consider the possible range of nuclear enrichment resulting from spallation due to cosmic rays produced by the central stars, with a focus on the isotope ^{26}Al . Young stellar objects — both protostars and pre-main-sequence stars — are observed to have substantial X-ray luminosities (Feigelson & Montmerle 1999), which is thought to coincide with comparable emission levels of energetic particles (cosmic rays). In the immediate vicinity of the star, this intense particle radiation can drive nuclear reactions through spallation and produce substantial quantities of radioactive nuclei.¹

In this context, the short-lived radioactive nuclei of interest have lifetimes of order ~ 1 Myr and can be produced with sufficient abundance to influence planetary properties. For example, radioisotopes of potential interest include ^{10}Be , ^{26}Al , ^{36}Cl , ^{41}Ca , ^{53}Mn , and others, which are thought to have been present in unexpectedly large numbers in the early formative stages of our own solar system (Lee et al. 1977; cf. Jura et al. 2013).

Radioactive nuclei, if present in sufficient abundances, can provide an important energy source during the planet formation process (see Urey 1955 to Reiter 2020). Sufficiently large planetesimals will melt due to their internal energy supply (Schramm 1971; Hevey & Sanders 2006), which leads to the differentiation of the rocky bodies (LaTourrette & Wasserburg 1998; Moskovitz & Gaidos 2011). After their formation is complete, the planets will have an additional luminosity source due to internal radioactivity. This additional heating can remove volatile components from both the raw materials and the planets themselves (Grimm & McSween 1993; Ikoma et al. 2018). More specifically, radioactive heating acts to dehydrate planetesimals (Lichtenberg et al. 2019) and thus affects the water content of forming planets. Radioactive nuclei also provide a significant source of ionization (especially in the outer disk; Cleeves et al. 2013), which in turn affects both the chemical composition of the disk and possibility of driving disk accretion through the magneto-rotational-instability.

A great deal of previous work has focused on the radioactive enrichment of our solar system, where meteoritic evidence indicates that the early solar nebula was enriched in SLRs relative to abundances expected in the interstellar medium (Lee et al. 1977; Wasserburg 1985). Such considerations place interesting constraints on the birth environment of the Sun (Adams 2010). One of the challenges facing such theoretical explanations is that we observe

¹For completeness we note that ‘spallation’ refers to nuclei being broken apart, whereas the production of ^{26}Al does not always break apart the target nuclei. Nonetheless, this paper follows standard usage in the astronomical literature where the term spallation refers to all nuclear reactions driven by particle radiation such as cosmic rays.

enhancements in several nuclear species, including ^{10}Be , ^{26}Al , ^{41}Ca , ^{60}Fe , ^{53}Mn , ^{107}Pd , and ^{129}I , and the relative abundances of the various nuclei must be accounted for (compare Shu et al. 1997; Lee et al. 1998; Gounelle et al. 2001; Goswami et al. 2001; Leya et al. 2003; Duprat & Tatischeff 2007; Liu & McKeegan 2009; Desch et al. 2010; Gounelle et al. 2013; Sossi et al. 2017; Jacquet 2019). In the present application, however, we are primarily concerned with the nuclear species that provide the most significant source(s) of ionization and heating. The expected time scales for both planet formation and disk evolution fall in the range 1 – 10 Myr, so that nuclei with half-lives longer than ~ 10 Myr are of less interest. Since ^{60}Fe must be produced via stellar nucleosynthesis, it is not considered here. The abundances of other nuclear species are relatively low, with the mass fraction of ^{26}Al larger than ^{36}Cl by a factor of ~ 4 and larger than ^{53}Mn by a factor of ~ 10 , so that the isotope ^{26}Al is likely to provide the largest impact. This treatment thus focuses on the production of ^{26}Al (but other isotopes that can be synthesized through spallation can be scaled from these results).

In this paper, we present a scenario for the production of cosmic radiation in the inner regions of disks associated with young stellar objects (Section 2). Through spallation reactions, this particle radiation can enrich the rocky material that eventually forms planets, where the enrichment levels are estimated in Section 3. For planets forming in disk regions near $r \sim 0.1$ AU, we find that the abundances of SLRs can be significantly enhanced relative to those inferred for our solar system (which are already thought to be relatively large). This additional source of heating and ionization can affect young and forming planets, as briefly outlined in Section 4. The paper concludes in Section 5 with a summary of results and a discussion of their implications.

2. Production of Particle Radiation

In the astrophysical scenario considered here, the production of particle radiation (cosmic rays) takes place near the magnetic truncation radius of the inner disk. In this region, the magnetic fields experience reconnection events which act to accelerate particles to high energies, thus creating a local flux of cosmic rays. This section outlines the basic properties for this source of particle radiation (for further detail, see Shu et al. 1996, 1997; Lee et al. 1998; Shu et al. 2001; Gounelle et al. 2001; Leya et al. 2003; Duprat & Tatischeff 2007; and references therein).

Young stellar objects, both protostars and T Tauri stars, are observed to have strong magnetic fields with typical surface values of order $B_* \approx 1 - 2$ kilogauss (Johns-Krull 2007). Near the star, these fields have enough pressure to control the inward accretion flow from the disk. As a result, the disk is truncated at the radius where the field pressure balances

the ram pressure due to accretion. The resulting truncation radius r_X can be written in the form

$$r_X = \omega_x \left(\frac{B_*^4 R_*^{12}}{GM_* \dot{M}^2} \right)^{1/7}, \quad (1)$$

where B_* is the field strength on the surface of the star, R_* is the stellar radius, M_* is the stellar mass, and \dot{M} is the mass accretion rate (from the disk onto the star, at the truncation point). The general form of this expression follows from dimensional analysis, whereas the dimensionless parameter ω_x varies with the details of the model (Ghosh & Lamb 1978; Blandford & Payne 1982; Najita & Shu 1994), but is expected to be of order unity. We are also implicitly assuming that the stellar magnetic field has a substantial dipole component.

In this scenario, mass accretes through the circumstellar disk and flows inward to the truncation radius given by equation (1), where the magnetic pressure becomes larger than the ram pressure of the flow. Gas parcels can accrete along the field lines and eventually reach the stellar surface, whereas rocky bodies of sufficient size are left behind in the disk region surrounding the radius r_X . The magnetic coupling between the star and disk acts to enforce a time-averaged rotation rate for the star that matches the Keplerian rotation rate at r_X . Both the accretion flow and the magnetic field lines are subject to fluctuations. As a result, the magnetic field in the truncation region is expected to wind up, and then reconnect, and thereby produce stressed fields and sporadic energy release, which in turn leads to both X-ray emission and particle acceleration. The net result of this star/disk coupling is the production of a particle luminosity L_p that is a substantial fraction of the photon luminosity L_* (Lee et al. 1998). Moreover, L_p is expected to be comparable to (but somewhat less than) the X-ray luminosity L_X (Padovani et al. 2016), which has been observed for a collection of young stellar objects (Feigelson et al. 2005; Preibisch et al. 2005). As a result, we expect the cosmic ray luminosity, the X-ray luminosity, and the stellar luminosity to obey the ordering relation

$$L_p \sim 10^{-1} L_X \sim 10^{-4} L_*. \quad (2)$$

The stellar luminosity $L_* \sim 1L_\odot$ for typical pre-main sequence stars (but is somewhat larger for protostellar objects). Note that lower mass stars have smaller main-sequence luminosities, but evolve more slowly via PMS contraction, and these effects tend to cancel out. Finally, we note that the particle luminosity L_p includes protons, alpha particles, and ^3He nuclei.

In this model, the cosmic ray luminosity is generated in the disk region near the truncation radius r_X . Here we assume that the annulus defined by $r_X/2 \lesssim r \lesssim r_X$ provides the bulk of the cosmic ray flux (see Najita & Shu 1994; Shu et al. 1997). Furthermore, the mass accretion rate and other parameters appearing in equation (1) vary with time, so that the outer boundary (at r_X) moves inward and outward, perhaps varying by a factor of 2. This annular region is coincident with that of X-ray emission, where observations suggest that

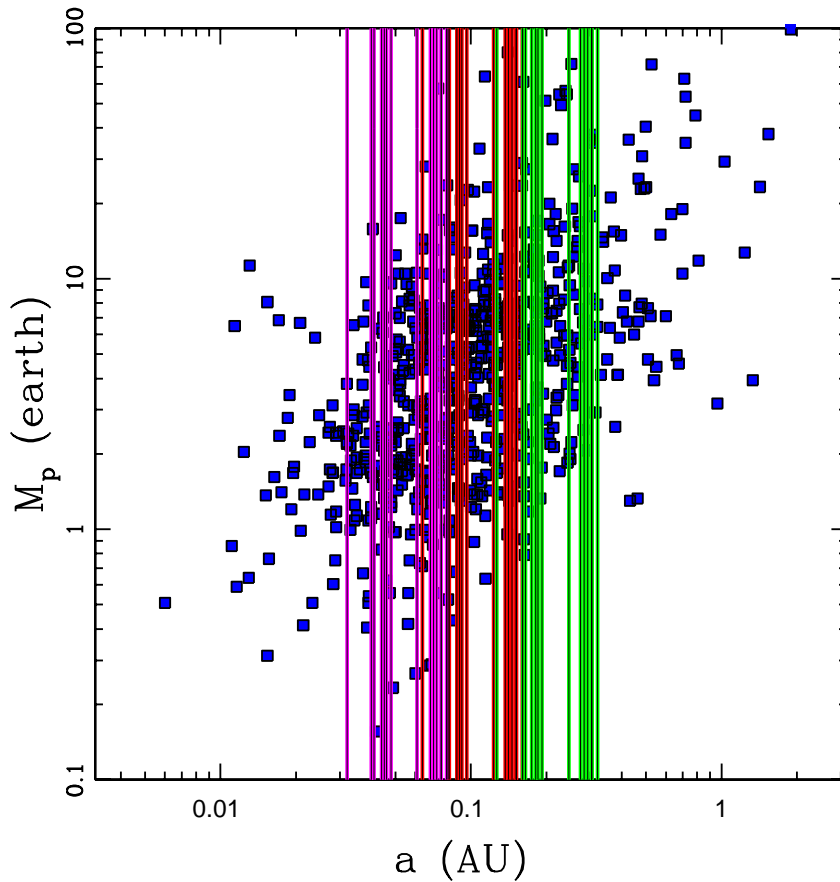


Fig. 1.— Estimated locations of magnetic truncation radius in observed T Tauri star/disk systems and the exoplanet population. The background points depict observed exoplanets in the current data base for systems containing 3 or more planets. The red vertical lines show the estimated location of the magnetic truncation radius for a sample of 15 T Tauri stars with observed magnetic field properties. Additional lines show magnetic truncation radii that are a factor of two larger (green) and smaller (magenta) than the fiducial values.

the plasma in the immediate vicinity of the reconnection events has a column density of order $\sim 10^{-4}$ g cm $^{-2}$ (Shu et al. 1997; Lee et al. 1998). This low column density implies that the cosmic rays flux produced alongside the X-rays will not be highly attenuated before interacting with rocky material in the region.

Within the reconnection annulus, cosmic rays are tied to the local magnetic fields, which are twisted and chaotic. Particle propagation is controlled by two important length scales. The first is the scale height of the inner disk, $H \sim r_X/20$, which determines the typical length scale of the tangled magnetic field. The second is the magnetic gyroradius $r_g = \gamma m c v / q B$, where $r_g \ll H$ for the particle energies and field strengths of interest. The following picture emerges: The cosmic rays are free to move along the field lines, which are highly convoluted with step length $\sim H$. The particles are closely tied to the field lines and thus experience little perpendicular propagation. In order to escape the reconnection region, the cosmic rays must travel a net distance of order r_X . Since the particles execute a random walk with step length H , the total distance d traveled to escape is given by $d \sim r_X^2 / H \sim 20 r_X$. As the cosmic rays travel through such a long distance, and cross the midplane of the disk multiple times, a large fraction of the particles will interact with rocky material located within the annulus.

The cosmic ray luminosity L_p corresponds to all particles with energy above some minimum value, $E \geq E_0$, where $E_0 \sim 10$ MeV. The cosmic rays with energy above this benchmark value are expected to have a power-law spectrum, which can be written in the form

$$\frac{df}{dE} = \frac{p-1}{E_0} \left(\frac{E}{E_0} \right)^{-p}, \quad (3)$$

where the index p depends on the source (Van Hollebeke et al. 1975; Reames et al. 1997, 1999; Mewaldt et al. 2012; Reames 2013). For cosmic radiation emitted by the Sun through the action of gradual flaring activity, the power-law index $p \approx 2.7$. The Sun also accelerates cosmic rays through the action of impulsive flares, which result in a steeper index $p \approx 3.5$. Galactic cosmic rays have a similar power-law index at high energies. Given this range of possibilities, for the sake of definiteness we adopt $p = 3$ for the estimates of this paper. Note the the distribution of equation (3) is normalized such that $\int_{E_0}^{\infty} (df/dE) dE = 1$.

The cosmic ray luminosity L_p is defined in terms of the energy emitted in particles. In order to determine the reaction rates for spallation, we also need to determine the rate \dot{N} of particle emission. With the cosmic ray spectrum (3) specified, we can define the luminosity density L_E in cosmic rays and the corresponding quantity \dot{N}_E for particle number according to

$$L_E = L_p \frac{p-2}{E_0} \left(\frac{E}{E_0} \right)^{1-p} \quad \text{and} \quad \dot{N}_E = \frac{L_p (p-2)}{E_0^2} \left(\frac{E}{E_0} \right)^{-p}. \quad (4)$$

These distributions are normalized such that

$$\int_{E_0}^{\infty} L_E dE = L_p, \quad \int_{E_0}^{\infty} \dot{\mathcal{N}}_E dE = \dot{\mathcal{N}}, \quad \text{and} \quad \dot{\mathcal{N}} = \frac{p-2}{p-1} \frac{L_p}{E_0}. \quad (5)$$

We can also specify the particle luminosity and particle emission rate for cosmic rays with energy above a threshold value, $E > E_{th} > E_0$,

$$L(E > E_{th}) = \left(\frac{E_0}{E_{th}} \right)^{p-2} L_p \quad \text{and} \quad \dot{\mathcal{N}}(E > E_{th}) = \left(\frac{E_0}{E_{th}} \right)^{p-1} \dot{\mathcal{N}}. \quad (6)$$

In addition to protons, the locally produced cosmic ray luminosity contains alpha particles (^4He nuclei), helions (^3He nuclei), and a small fraction of larger nuclei. For the sake of definiteness, we assume here that the values for $\dot{\mathcal{N}}$ given above correspond to the particle output in protons and alpha particles, which make up the majority of particles accelerated from the reconnection region. We further assume that the emission rate for alpha particles is smaller by an order of magnitude, so that $\dot{\mathcal{N}}_\alpha = 0.1\dot{\mathcal{N}}$ and $\dot{\mathcal{N}}_p = 0.90\dot{\mathcal{N}}$. This assumption is consistent with both the cosmic abundance of helium and that content of galactic cosmic rays. We then consider an admixture of helions h (^3He), where the relative number of particles is more uncertain. For galactic cosmic rays, the ratio $[h/\alpha]$ is typically $\sim 1/10$ (Formato et al. 2014). On the other hand, the ratio $[h/\alpha]$ can approach and even exceed unity in the most energetic solar flares (Garrard et al. 1973; Fisk 1978). Here we adopt an intermediate value by considering the additional luminosity of helions to be given by $\dot{\mathcal{N}}_h = 0.03\dot{\mathcal{N}}$.

The magnetic field strengths and other parameters appearing in equation (1) have been measured for a collection of T Tauri stars (Johns-Krull 2007), allowing us to estimate the expected values of the truncation radius r_X . The resulting values are shown in Figure 1, where they are plotted alongside the observed exoplanets found in multi-planet systems (see Batalha et al. 2011 and subsequent work), where estimates of the planet masses are plotted as a function of semimajor axis. The vertical red lines depict the locations of the radii r_X for the 15 T Tauri stars in the observed sample and for dimensionless parameter $\omega_x = 1$. Since the mass accretion is episodic, and its rate \dot{M} can vary by an order of magnitude, the truncation radius r_X can vary by (at least) a factor of two. Other parameters (including ω_x) can also vary. To account for this diversity, Figure 1 also shows the locations of the truncation radii that are a factor of two larger (green lines) and a factor of two smaller (magenta lines) than their fiducial values. The locations of the magnetic truncation radii thus coincide with the radial locations of observed exoplanets. Since the particle radiation (outlined above) originates within this same region, this class of exoplanets will be exposed to intense cosmic ray radiation during their early evolutionary stages.

The young stars used to determine the magnetic truncation radii in Figure 1 and the (older) host stars of the planetary systems have comparable properties. Specifically, the sample of T Tauri stars (Johns-Krull 2007) has a distribution of masses that can be characterized by $M_* = 0.72 \pm 0.45 M_\odot$ (in the form of mean \pm standard deviation). The host stars for the planetary sample shown in the figure have comparable masses, which fall in the range $M_* = 0.10 - 1.35 M_\odot$. The resulting values for the magnetic truncation radii are $r_X = 0.11 \pm 0.034$ AU. Finally, the corresponding X-ray luminosities are also measured for the T Tauri sample, where $L_X = 1.53 \pm 1.32 \times 10^{-3} L_\odot$. These values define a characteristic particle luminosity $L_p = 0.1 L_X \approx 1.5 \times 10^{-4} L_\odot$, which corresponds to $\dot{N} = 3.75 \times 10^{34}$ particle/sec.

3. Irradiation of Rocky Targets by Local Cosmic Rays

The previous section outlined the model for the generation of cosmic rays in the annular region near the truncation radius r_X . For planets forming in this region, this section estimates how spallation reactions can enrich the raw materials with radioactive nuclei. The spallation reactions act on target nuclei and generate radioactive isotopes. The reactions of interest have the general form



where T is the target nucleus, P_{SLR} is the radioactive product, and χ is the projectile (a proton p , alpha particle α , or helion h). The ξ_j represent the additional particles that are produced, generally protons p , neutrons n , and alphas α with varying numbers per reaction. Here we focus on the radioactive products $P_{SLR} \sim {}^{26}\text{Al}$.

The target nuclei of interest generally reside in rocky bodies of various sizes. In the current paradigm of planet formation, dust grains (with characteristic size $R \sim 0.1 - 1 \mu\text{m}$) grow into larger rocky bodies known as pebbles (with characteristic size $R \sim 0.1 - 1$ cm). After the concentration of pebbles becomes large enough, a streaming instability (Youdin & Goodman 2005; Drazkowska et al. 2016) or some other process consolidates the pebbles into much larger bodies called planetesimals with characteristic size $R \sim 10 - 100$ km (Simon et al. 2016). These planetesimals subsequently accumulate into full-sized planets. This paper focuses on the formation of rocky planets with masses in the range $M_{\text{plan}} = 1 - 10 M_\oplus$. Larger planets can sometimes form, where rocky cores of mass $M_c \sim 10 M_\oplus$ accrete gaseous envelopes and reach Jovian masses. However, such hot Jupiters are relatively rare in the reconnection region, and are not addressed in this work.

3.1. Cosmic Ray Exposure in the Optically Thin Regime

In the scenario under consideration (Section 2), magnetic fields from the star truncate the circumstellar disk at radius r_X and cosmic rays are generated in the surrounding region. The resulting number flux Φ_{CR} in cosmic rays in the reconnection annulus is thus given by

$$\Phi_{CR} \approx \frac{\dot{\mathcal{N}}}{\pi r_X^2}, \quad (8)$$

where $\dot{\mathcal{N}}$ is the total number of cosmic rays emitted per unit time.

We first consider a particular spallation reaction operating in the optically thin regime. The rate Γ at which a target nucleus absorbs cosmic rays, and thereby produces a radioactive isotope, can be written in the form

$$\Gamma_k = \frac{1}{\pi r_X^2} \int_{E_0}^{\infty} \dot{\mathcal{N}}_E \sigma_k(E) dE \equiv \frac{\dot{\mathcal{N}}_k \langle \sigma \rangle_k}{\pi r_X^2}, \quad (9)$$

where $\sigma_k(E)$ is the cross section for the reaction of interest and $\langle \sigma \rangle_k$ is the cross section averaged over the distribution of cosmic ray energies. The index k labels the reaction of interest. Note that the total cosmic ray luminosity $\dot{\mathcal{N}}$ (in particle number) includes projectiles of all types, whereas the only a fraction $\dot{\mathcal{N}}_k$ participate in the reaction.

In this application, we are interested in the amount of ^{26}Al produced, which can be synthesized through a number of spallation reactions. Specifically, reactions involving targets of ^{27}Al , ^{26}Mg , and ^{28}Si are important for proton spallation, and targets of ^{26}Mg and ^{28}Si are relevant for alpha particle radiation. Targets of ^{24}Mg , ^{25}Mg , ^{27}Al , and ^{28}Si are relevant for spallation with helion (^3He) particles. These reactions are summarized in Table 1, along with defining parameters of interest (defined below).

The abundance of ^{26}Al is measured relative to a reference isotope, taken here to be ^{27}Al . Over a given exposure time t_{exp} , the abundance ratio is given by the sum

$$\mathcal{R}_{26} = \frac{X_{26}}{X_{27}} \approx \frac{\dot{\mathcal{N}} t_{\text{exp}}}{\pi r_X^2} \sum_k \langle \sigma \rangle_k \frac{X_k}{X_{27}} \frac{\dot{\mathcal{N}}_k}{\dot{\mathcal{N}}}. \quad (10)$$

The first factor in the sum accounts for the cross section of the interaction, the second factor is the ratio of abundances of the target nuclei, and the third factor is the ratio of abundances of the projectiles.

Note that the above treatment represents an upper limit on the expected abundance ratio. The estimate does not include the back reaction on the SLR production rate due to the loss of target nuclei or the decay of the radioactive products. If the value of \mathcal{R}_{26}

approaches unity, then the ratio will be smaller than assumed here due to the decline in the supply of targets, although this correction is small. In addition, however, if the exposure time t_{exp} become comparable to the decay time of the SLR, then the ratio of SLRs will be smaller due to radioactive decay (which occurs at the rate $\lambda = \ln 2/t_{1/2}$). Taking into account both of these complications, we can generalize the result (10) to obtain

$$\mathcal{R}_{26} = \frac{\dot{\mathcal{N}}\langle\sigma\rangle_T}{\pi r_X^2} \frac{1}{\lambda - \Gamma} [1 - e^{-(\lambda - \Gamma)t_{\text{exp}}}] \rightsquigarrow \frac{\dot{\mathcal{N}}\langle\sigma\rangle_T}{\pi r_X^2 \lambda}, \quad (11)$$

where we have defined a total effective cross section

$$\langle\sigma\rangle_T \equiv \sum_k \langle\sigma\rangle_k \frac{X_k}{X_{27}} \frac{\dot{\mathcal{N}}_k}{\dot{\mathcal{N}}}. \quad (12)$$

Note that we expect $\lambda \gg \Gamma$. In the limit of short exposure times, specifically $t_{\text{exp}} \ll t_{1/2}$, we recover equation (10). In the opposite limit where $t_{\text{exp}} \gg t_{1/2}$, we find that $\mathcal{R}_{26} \rightarrow \Gamma/(\lambda - \Gamma) \approx \Gamma/\lambda$. In other words, the effective exposure time becomes $t_{\text{exp}} \sim \lambda^{-1} = t_{1/2}/\ln(2)$.

Nuclear Reactions for Spallation

| Reaction | Cross Section $\langle\sigma\rangle$ (mb) | Target Abundance X_T/X_H | Projectile Fraction $\dot{\mathcal{N}}_X/\dot{\mathcal{N}}$ |
|------------------------------------------------------|----------------------------------------------|-------------------------------|----------------------------------------------------------------|
| $^{26}\text{Mg}(p, n)^{26}\text{Al}$ | 417 | 4.6×10^{-6} | 0.9 |
| $^{27}\text{Al}(p, pn)^{26}\text{Al}$ | 44 | 3.5×10^{-6} | 0.9 |
| $^{28}\text{Si}(p, 2pn)^{26}\text{Al}$ | 7.9 | 3.8×10^{-5} | 0.9 |
| $^{24}\text{Mg}(\alpha, pn)^{26}\text{Al}$ | 30 | 3.3×10^{-5} | 0.1 |
| $^{28}\text{Si}(\alpha, \alpha pn)^{26}\text{Al}$ | 4.4 | 3.8×10^{-5} | 0.1 |
| $^{24}\text{Mg}(^3\text{He}, p)^{26}\text{Al}$ | 216 | 3.3×10^{-5} | 0.03 |
| $^{25}\text{Mg}(^3\text{He}, pn)^{26}\text{Al}$ | 316 | 4.2×10^{-6} | 0.03 |
| $^{27}\text{Al}(^3\text{He}, \alpha)^{26}\text{Al}$ | 33 | 3.5×10^{-6} | 0.03 |
| $^{28}\text{Si}(^3\text{He}, p\alpha)^{26}\text{Al}$ | 60 | 3.8×10^{-5} | 0.03 |

Table 1: Nuclear spallation reactions for the production of ^{26}Al . The reactions are grouped according to proton reactions (top), alpha reactions (middle), and helion reactions (bottom). The second column presents the cross section averaged over the normalized cosmic ray spectrum. The relative abundances of the target nuclei (Lodders 2003) and the projectiles are listed in the last two columns (see text).

This treatment uses the spallation cross sections provided by the TENDL Nuclear Data Library (Koning et al. 2019). The tabulated cross sections listed in Table 1 are averaged over

the (normalized) spectrum of cosmic rays, where we use $p = 3$ as the index. The resulting values are given in Table 1. Note that the experimentally determined cross sections show significant variations in their published values (compare these values with Soppera et al. 2020a,b,c, and with the weighted-averaged values given in Lee et al. 1998²). The overall uncertainty in the cross sections is less than a factor of two. Moreover, the values used here (Koning et al. 2019) tend to be smaller than those of the other sources, especially at higher cosmic ray energy, so that the estimates of this paper represent lower limits. The abundances of the target nuclei are assumed to have solar values (taken from Lodders 2003). Finally, the relative fractions of projectiles (p, α, h) are presented in the last column of the table (see Section 2).

With the specifications given above, the total spallation cross section for ²⁶Al production defined by equation (12) becomes $\langle\sigma\rangle_T \approx 740$ mb. It is useful to define the benchmark value of abundance ratio

$$\mathcal{R}_{26}^* = 0.12 \left(\frac{\dot{N}}{3.75 \times 10^{34} \text{ s}^{-1}} \right) \left(\frac{r_X}{0.1 \text{ AU}} \right)^{-2} \left(\frac{\langle\sigma\rangle_T}{740 \text{ mb}} \right). \quad (13)$$

At the expected location $r_X \sim 0.1$ AU, this benchmark value of the nuclear abundance ratio is much larger than the measured value in solar system meteorites. However, this large ratio can only be realized for moderate amounts of rocky material that is exposed to particle radiation under optically thin conditions over long times. In practice, energy losses within the rocky bodies reduces the abundance ratio by a substantial factor. Departures from this idealized limit are considered in the following section.

3.2. Optical Depth Considerations

In general, the target nuclei could reside in a gaseous phase, be locked up in dust grains, or be incorporated in larger rocks. Within the current paradigm of planet formation, we expect most of the targets of interest to condense onto dust grains or larger bodies. The exposure of the targets to the cosmic ray flux is limited in two stages. First, the cosmic ray flux can be attenuated on its path to the rocky entities. Second, the cosmic ray flux is attenuated further as it propagates within the rocky material. In the scenario considered here, the plasma in the reconnection region is optically thin (see the previous section) so that the first type of attenuation occurs through interactions with the sea of rocky bodies. Once the cosmic ray flux reaches the surface of a given rock, additional attenuation of the cosmic rays takes place within the body itself.

²Note that this reference uses different weighting of the cross sections with cosmic ray energy.

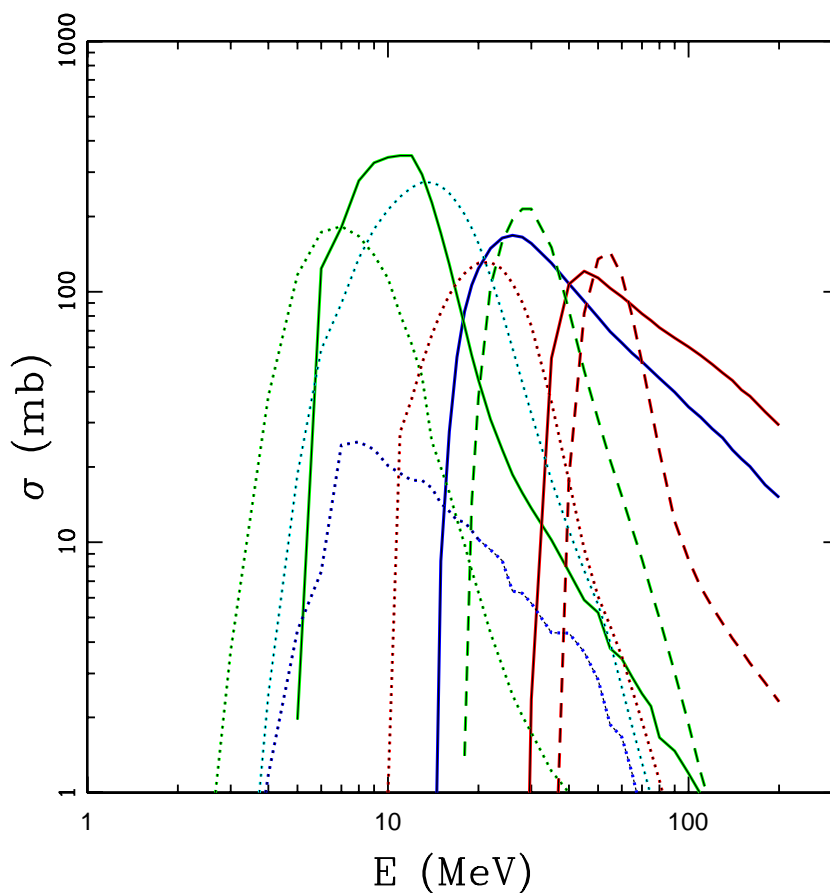


Fig. 2.— Cross sections for spallation reactions (from Koning et al. 2019). The solid curves show the cross sections of reactions with protons for target nuclei ^{26}Mg (green), ^{27}Al (blue), and ^{28}Si (red). The dashed curves show the cross sections of reactions with alpha particles for target nuclei ^{24}Mg (green) and ^{28}Si (red). The dotted curves show the cross sections of reactions with neutrons for target nuclei ^{24}Mg (green), ^{25}Mg (cyan), ^{27}Al (blue), and ^{28}Si (red).

Consider a total mass M_R of rocky material distributed across the reconnection annulus, so that the column density of the region is given by

$$\Sigma_{\text{rock}} = \frac{M_R}{\pi r_X^2} \approx 850 \text{ g cm}^{-2} \left(\frac{M_R}{M_\oplus} \right) \left(\frac{r_X}{0.1 \text{ AU}} \right)^{-2}. \quad (14)$$

Here we consider the regime where the rocky bodies with radius R are partially optically thick. As a result, the constituent nuclei are exposed to a fraction \mathcal{F} of the cosmic ray flux that strikes the surface, and a corresponding fraction $1 - \mathcal{F}$ of the flux is absorbed. Note that the fraction depends on the rock size, $\mathcal{F} = \mathcal{F}(R)$, and this function is estimated below. The optical depth of the reconnection annulus is given by

$$\tau_{\text{rock}} = \Sigma_{\text{rock}} \frac{3}{4\rho R} [1 - \mathcal{F}(R)], \quad (15)$$

where $\rho \approx 3.3 \text{ g cm}^{-3}$ is the density of the rocks. As a rough approximation, we can determine the fraction of the original cosmic ray flux that is incident on the rocky bodies by using a simple one-dimensional slab geometry. This fraction is reduced further within the rocks, so that the nuclei are exposed to an overall fraction f_τ of the flux given by

$$f_\tau = \frac{1}{\tau_{\text{rock}}} [1 - e^{-\tau_{\text{rock}}}] \mathcal{F}(R). \quad (16)$$

The first part of the expression accounts for the attenuation of the cosmic ray flux by the background sea of rocky material, before the flux reaches the surface of a given rock. The final factor $\mathcal{F}(R)$ accounts for the fraction of original surface flux that reaches nuclei within the rock.

We thus need to estimate $\mathcal{F}(R)$. The cosmic rays entering the rocky bodies lose energy in two ways: They can interact with nuclei and drive nuclear reactions such as spallation. The interaction cross sections for such processes are of order $\sigma \sim 10^{-25} \text{ cm}^2$. They can also lose energy through Coulomb interactions with electrons in the rock. In this case, the cosmic rays continually lose energy and eventually come to a stop after encountering a sufficient column density of material. For cosmic rays with incident energy $E \sim 10 \text{ MeV}$, the required stopping column density $\Sigma_s \sim 0.3 \text{ g cm}^{-2}$ (Reedy & Marti 1991; Reedy 2015). This stopping criterion corresponds to an effective interaction cross section given by $\sigma_{\text{eff}} \sim Am_p/\Sigma_s \sim 10^{-22} \text{ cm}^2$, where m_p is the proton mass, and A is the mean atomic mass number of the rocky material. Note that cosmic rays with higher energy have a larger stopping column. Nonetheless, cosmic rays lose their energy within rocks more readily than they interact with nuclei through spallation.

As cosmic rays propagate through the rocky material, the loss of energy is given by the expression

$$\frac{dE}{ds} = -F \left(\frac{E_{th}}{E} \right)^q, \quad (17)$$

where the power-law index $q \approx 0.7$ and the coefficient F depends on the composition of the target and the type of cosmic ray particle (Reedy & Marti 1991). In addition, the coefficient is scaled such that the benchmark energy E_{th} is the threshold energy for the reaction of interest. This loss equation can then be integrated to find the energy of the particle remaining as a function of the distance s traveled,

$$E(s) = [E_i^{q+1} - (q+1)F E_{th}^q s]^{1/(q+1)}. \quad (18)$$

Since the cosmic ray energy spectrum is much steeper than the energy dependence $\sigma(E)$, we can make the approximation that the cross sections are relatively constant above a threshold energy E_{th} . In order for a cosmic ray to have sufficient energy to interact after traveling a distance s , $E(s) > E_{th}$, and the initial energy E_i must be larger than the value

$$E_i > E_{th} [1 + (q+1)(F/E_{th})s]^{1/(q+1)}. \quad (19)$$

Suppose that a flux of particles Φ_0 is incident on the rocky surface. For the assumed cosmic ray energy spectrum from equation (3), the flux of particles with energy larger than a given energy E can be written in the form

$$\Phi(> E) = \Phi_0 \left(\frac{E_0}{E} \right)^{p-1}. \quad (20)$$

The flux of particles above the threshold energy, evaluated at a distance s into the rocky material, is thus given by

$$\Phi(s) = \Phi_0 \left(\frac{E_0}{E_{th}} \right)^{p-1} [1 + (q+1)(F/E_{th})s]^{-(p-1)/(q+1)}. \quad (21)$$

The leading factor represents the incident flux of particles with sufficient energy to induce spallation reactions. The factor in square brackets determines how the flux is attenuated with the distance s traveled through the rock.

Next we want to determine the effective cosmic ray flux impinging on the target nuclei within a rocky body. For simplicity, the rocks of interest can be considered as uniform density spheres of radius R . Within the reconnection region, the cosmic ray flux can be considered as isotropic. This isotropic flux of particle is thus incident on a spherical rock. For a given position within the rock (r, μ) , where r is the spherical radial coordinate and the $\mu = \cos \theta$, the distance coordinate s is given by

$$s = r\mu + [R^2 - r^2(1 - \mu^2)]^{1/2}. \quad (22)$$

It is useful to make the following definitions,

$$\ell_0 = \frac{E_{th}}{(q+1)F}, \quad \gamma = \frac{p-1}{q+1}, \quad \text{and} \quad \xi = \frac{r}{R}, \quad (23)$$

where $\ell_0 \approx 0.1$ cm for $E_{th} = 10$ MeV. The target nuclei within the rock receive a only fraction \mathcal{F} of the original isotropic flux striking the surface, where

$$\mathcal{F}(R) = \frac{3}{2} \left(\frac{\ell_0}{R} \right)^\gamma \int_0^1 \xi^2 d\xi \int_{-1}^1 d\mu \left[(\ell_0/R) + \xi\mu + [1 - \xi^2(1 - \mu^2)]^{1/2} \right]^{-\gamma}. \quad (24)$$

In the limit of small rocky bodies $R \ll \ell_0$, the fraction $\mathcal{F} \rightarrow 1$ as expected. Moreover, the quantity $1 - \mathcal{F} \sim \mathcal{O}(R/\ell_0)$ in this regime. In the opposite limit $R \gg \ell_0$, the fraction decreases rapidly with increasing R . In general, we must evaluate the integrals in equation (24) numerically.

3.3. Nuclear Abundance Estimates

The considerations outlined above can be summarized by writing the nuclear abundance ratio for ^{26}Al in the form

$$\mathcal{R}_{26} = \frac{\dot{\mathcal{N}}\langle\sigma\rangle_T}{\pi r_X^2 \lambda} [1 - e^{-\lambda t_{\text{exp}}}] \left[\frac{1 - e^{-\tau}}{\tau} \right] \mathcal{F}(R). \quad (25)$$

The leading factor corresponds to the case where the target nuclei experience exposure from an unattenuated cosmic ray flux in the long-term limit under optically thin conditions. The first dimensionless correction factor in square brackets takes into account departures from saturation due to shorter exposure times. The second factor accounts for the attenuation of the cosmic ray flux before it reaches the surfaces of the rocky bodies, where the optical depth of the reconnection region is given by $\tau \approx \tau_{\text{rock}}$ (see equation [15]). The final factor results from energy loss of the cosmic flux within the rocky entities, primarily due to Coulomb interactions, as approximated using the fraction \mathcal{F} from equation (24).

The resulting estimates for the abundance ratio \mathcal{R}_{26} are shown in Figure 3 as a function of the radius R of the rocky bodies. Results are shown for a range of surface densities Σ_{rock} , which sets the level of the optical depth and depends on the total mass of rocky material in the reconnection region (see equation [14]). Curves are shown for total masses corresponding to the planet types of interest, specifically $M_R = 0.5M_\oplus$ (upper red curve), $1M_\oplus$ (orange), $2M_\oplus$ (green), $4M_\oplus$ (blue), and $8M_\oplus$ (lower magenta curve). These estimates are calculated in the long-time limit so that $\lambda t_{\text{exp}} \gg 1$, which is valid for exposure times of order 1 Myr or longer. For comparison, the lower dashed line shows the inferred abundance ratio for our solar system. Although the estimated abundance ratios are substantially larger than those of our solar system, they are also much smaller than the maximum benchmark value given by equation (13).

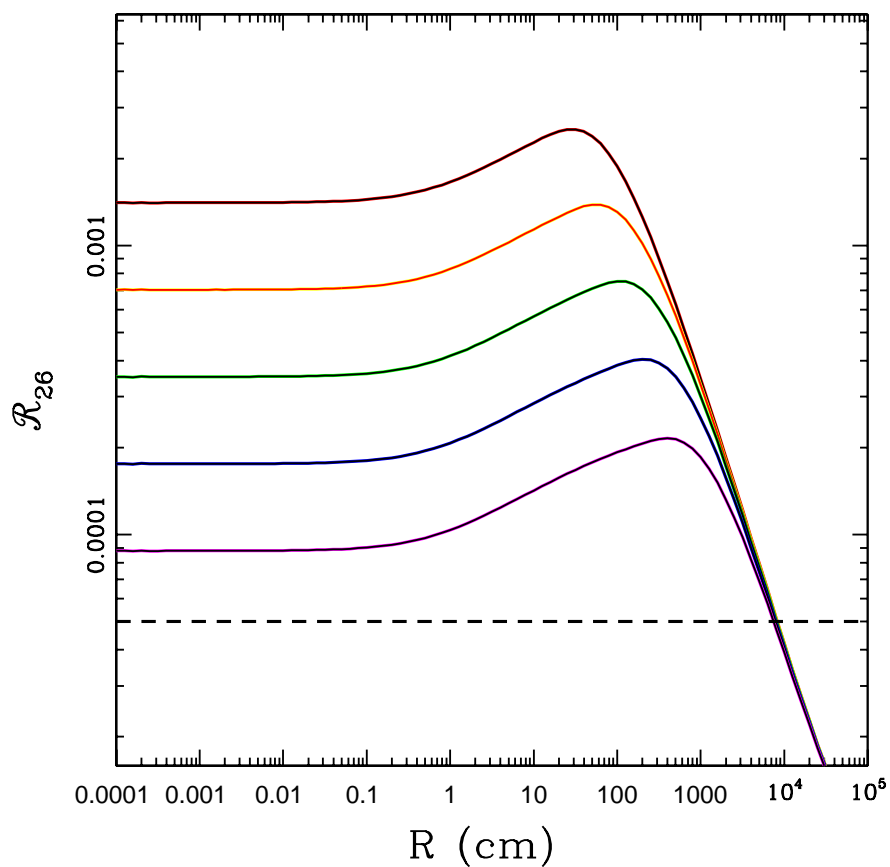


Fig. 3.— Estimated abundance ratio \mathcal{R}_{26} (for $^{26}\text{Al}/^{27}\text{Al}$) as a function of radius of rocky bodies. Curves are shown for different amounts of rocky material in the reconnection annulus, corresponding to increasing mass from top to bottom: $M_R/M_\oplus = 1/2$ (red), 1 (orange), 2 (green), 4 (blue), and 8 (magenta). The lower dashed line marks the abundance ratio inferred for our solar system.

In the limit where the rocky bodies are small, the curves in Figure 3 are flat and depend only on the total optical depth of the reconnection region (see equation [15]). In this regime, the quantity $(1 - \mathcal{F})/R \rightarrow \text{constant} \sim 1/\ell_0$, so attenuation of the cosmic rays depends only on the total amount of material (independent of R). Notice also that most of the attenuation results from Coulomb effects, rather than nuclear reactions. As the radius R increases, the optical depth τ_{rock} of the background rocky material decreases. The reconnection region becomes optically thin for rock sizes $R \gtrsim 200$ cm (M_R/M_\oplus). At the same time, the optical depth of each individual rock increases, with an increasing fraction of its interior shielded from the incident cosmic ray flux. The competition between these two effects results in the broad maximum shown for $R = 50 - 100$ cm. For even larger rock radii, the abundance decreases sharply as an increasing fraction of the constituent nuclei are shielded. The enrichment levels are less than solar system values for rock sizes $R \gtrsim 10^4$ cm, and become negligible for $R \gtrsim 1$ km.

For small planets, $M_{\text{plan}} \sim 1M_\oplus$, Figure 3 indicates that enrichment levels can be more than an order of magnitude larger than those inferred for the Solar System (equivalently, a maximum mass of $\sim 15M_\oplus$ of material can be enriched to Solar System values). In previous studies, which focus on meteoritic enrichment, the exposure times are often smaller than those considered here, with correspondingly smaller yields (see, e.g., Shu et al. 1996 to Sossi et al. 2017). Such studies also require the enriched material to be carried out to larger heliocentric distances. This scenario — which allows for rocky material to be exposed to the largest cosmic ray fluxes over the longest times — thus maximizes local enrichment. Nonetheless, given the finite number of energetic cosmic rays, there is a limit on the amount of material that can achieve such high abundances of ^{26}Al . Previous studies estimate that only $\sim 3M_\oplus$ of material can reach solar system abundances (Duprat & Tatischeff 2007), where this limit can be extended up to $\sim 10M_\oplus$ under favorable circumstance (Fitoussi et al. 2008). These results are comparable to the mass of $\sim 15M_\oplus$ found here (where we assume long exposure times, so that enrichment is saturated, and use a somewhat different treatment for Coulomb losses). Significantly, all of these estimates ($3 - 15M_\oplus$) fall below the estimated rocky inventory of the Solar System ($40 - 80 M_\oplus$). This finding suggests that spallation cannot enrich the entire early solar nebula to the high isotopic abundances observed in meteorites.

For typical pebble sizes $R \sim \text{few cm}$, the estimated abundance ratio has the approximate value $\mathcal{R}_{26} \approx 0.001 (M_R/M_\oplus)^{-1}$. For a planet with mass $M_{\text{plan}} \approx M_R = 1 M_\oplus$, for example, this enrichment level is ~ 15 times larger than that inferred for our solar system. Note that smaller bodies ($R \ll 1$ cm) are likely to be swept up into the accretion flow, deposited onto

the stellar surface, and be unavailable for planet formation.³ The key issue is thus the length of time t_{exp} that the pebbles remain small (~ 1 cm) before being incorporated into larger planetesimals. Next we note that radioactive heating rates, and other physical quantities of interest, depend on the mass fraction X_{26} of ^{26}Al , where

$$X_{26} = X_{27} \mathcal{R}_{26} \approx 4.5 \times 10^{-6} \left(\frac{M_R}{M_{\oplus}} \right)^{-1}. \quad (26)$$

Here we have taken X_{26} and X_{27} to be the mass fractions of the rocky material, and have used $X_{27} \approx 4.5 \times 10^{-3}$ for solar system material (estimated from Table 2 of Lodders 2003). Another quantity of interest is the power per unit volume \mathcal{H} due to radioactivity, given by

$$\mathcal{H} = \lambda \epsilon X_{26} \left(\frac{\rho}{26m_p} \right) e^{-\lambda t} \approx 0.066 \text{ erg s}^{-1} \text{ cm}^{-3} \left(\frac{M_R}{1M_{\oplus}} \right)^{-1} e^{-\lambda t}, \quad (27)$$

where $\epsilon \approx 4$ MeV is the energy deposited per decay of the ^{26}Al nucleus. The second approximate equality evaluates the volume heating rate for standard values of the parameters.

Given these estimates for radioactive enrichment levels, it is useful to assess how the results depend on the input parameters and other uncertainties. Figure 3 shows how the predicted ^{26}Al abundances vary with the size of the rocky bodies and the total optical depth of the reconnection region (given by the total mass in solids). These curves are calculated in the regime of long exposure times ($\lambda t_{\text{exp}} \gg 1$); shorter exposure times can be considered by including the dimensionless correction factor in equation (25). Additional input to the estimates include the reaction cross sections, the target abundances, the relative populations of cosmic ray species, and the power-law index of the particle radiation spectrum. All of these variables combine to specify the net cross section $\langle \sigma \rangle_T$ (see equation [10]). The cross sections for individual reactions $\langle \sigma \rangle_k$ averaged over the cosmic ray spectrum show little variation with the spectral index because the cross sections are relatively localized in energy (Duprat & Tatischeff 2007; Fitoussi et al. 2008; see also Figure 2). The target abundances scale with the metallicity (where solar values are used here). One uncertain quantity is the fraction of the cosmic ray flux in helions, taken here to be 0.03. This fraction could vary by factors of ~ 3 , but the helion contribution to the overall production rate is only 10.7%, so that the uncertainty in the ^{26}Al yield is also $\sim 10\%$. Perhaps the largest uncertainty is the net luminosity in energetic particles. The value used here, $L_p = 10^{-4} L_*$, provides a good estimate for the expectation value (Feigelson et al. 2005); however, the system to system scatter allows for an order of magnitude variation from the mean, with a corresponding variation in the expected radioactive yields.

³For example, Gounelle et al. (2001) use the size range $R \sim 100\mu\text{m} - 10$ cm for the cores of enriched rocks in our solar system.

4. Short-Lived Radionuclides in Planetesimals and Planets

Given the elevated levels of ^{26}Al enrichment expected for rocky bodies residing in the reconnection region, this section explores their effects on newly formed planetesimals and fully formed planets. Here we assume that small (~ 1 cm) bodies (pebbles) are irradiated by cosmic rays and attain a sizable inventory of radioactive nuclei. Streaming instability, or some alternate process, then produces much larger bodies (planetesimals) on a relatively short time scale. These larger entities, with sizes 10 – 100 km, are heated by radioactive decay. Here we estimate the relevant time scales and determine the circumstances under which these bodies can melt. If the planetesimals are readily incorporated into full-sized planets, then the planets themselves can have a substantial internal luminosity.

4.1. Equilibrium Time Scale

The time scale over which a planetesimal adjusts its internal thermal structure is governed by the Kelvin-Helmholtz time, i.e., the time required for the internal luminosity to radiate away the heat content of the planetesimal. The luminosity is given by $L_{\text{in}} = \mathcal{H}M/\rho$, where M is the mass of the rocky body. The heat content is given by $\mathcal{U} = CMT$, where C is the specific heat capacity of the rock. The characteristic cooling time scale is thus given by

$$t_{\text{cool}} = \frac{\mathcal{U}}{L_{\text{in}}} = \frac{C\rho T}{\mathcal{H}} \approx 27,000 \text{ yr} \left(\frac{\mathcal{H}}{0.066 \text{ erg s}^{-1} \text{ cm}^{-3}} \right)^{-1} \left(\frac{T}{2000 \text{ K}} \right). \quad (28)$$

The temperature reference scale is chosen because rock melts when $T \gtrsim 2000$ K. The resulting cooling time is substantially shorter than the decay time scale for the SLRs (~ 1 Myr). Note that this time scale is independent of the mass of the planetesimal.

4.2. Size Scale for Planetesimal Melting

The internal radioactive luminosity of the rocky body L_{in} must be transported outwards, so that the temperature obeys a diffusion equation of the general form

$$\rho C \frac{\partial T}{\partial t} = \frac{1}{r^2} \frac{\partial}{\partial r} \left(K_c r^2 \frac{\partial T}{\partial r} \right) + \mathcal{H}(r, t), \quad (29)$$

where $\mathcal{H}(r, t)$ is the heating due radioactivity and K_c is the thermal conductivity (see Hevey & Sanders 2006 and references therein). We can divide out the density ρ and the specific

heat C to obtain

$$\frac{\partial T}{\partial t} = \frac{\kappa}{r^2} \frac{\partial}{\partial r} \left(r^2 \frac{\partial T}{\partial r} \right) + \frac{\mathcal{H}_0 \kappa}{K_c} e^{-\lambda t}, \quad (30)$$

where \mathcal{H}_0 is a constant and $\kappa \equiv K_c/C\rho$ is the thermal diffusivity of the rocky material. If we assume that the initial temperature of the planetesimal is that of the ambient region at T_0 , then the initial condition $T(r, t = 0) = T_0$. Following standard treatments of this problem (Carslaw & Jäger 1959), the solution has the form

$$T(r, t) = T_0 + \frac{\mathcal{H}_0 \kappa}{\lambda K_c} e^{-\lambda t} \left[\frac{R \sin qr}{r \sin qR} - 1 \right] + \frac{\mathcal{H}_0 R^2}{K_c} \frac{R}{r} \sum_{n=1}^{\infty} a_n \sin \left(\frac{n\pi r}{R} \right) e^{-\kappa n^2 \pi^2 t / R^2}, \quad (31)$$

where we have defined

$$q \equiv \sqrt{\frac{\lambda}{\kappa}} \quad \text{and} \quad a_n \equiv \frac{2}{\pi^3} \frac{(-1)^n}{n(n^2 - \lambda R^2 / \kappa \pi^2)}. \quad (32)$$

The analytic solution (31) assumes that the thermal conductivity and diffusivity of the rock is constant. However, once the temperature is high enough to melt the rock, $T \gtrsim 2000$ K, the molten body can transport heat via convection and the thermal properties change.

Here we use the solution (31) to map out the parameter space for which planetesimals can melt. For a given value of the radioactive heating rate \mathcal{H}_0 , we find the minimum planetesimal size R that is required to achieve a given temperature. For the sake of definiteness, we measure the heating rate in terms of the benchmark value $\mathcal{H}_{SS} = 6.4 \times 10^{-3} \text{ erg s}^{-1} \text{ cm}^{-3}$ that is often used for planetesimals in our solar system.⁴ In addition, we require that 90 percent of the radial extent of the planetesimal reach the given temperature. Figure 4 shows the resulting contours of constant temperature in the plane of size R versus heating rate \mathcal{H}_0 . The curves correspond to temperatures from $T = 1000$ K (red) up to $T = 5000$ K (magenta), with the dashed curves showing intermediate temperature values. The expected temperature required for melting of rock is about 2000 K, as depicted by the green curve in the Figure. As a result, planetesimals are expected to become almost fully molten for the parameter space above the green curve.

For the relatively large radioactive heating rates of interest, $t_{\text{cool}} < t_{1/2}$, so that the temperature structure of the planetesimal can reach an equilibrium state. As a result, the steady-state solution of the diffusion equation (29) is applicable and takes the form

$$T(r) = T_S + T_x \left(1 - \frac{r^2}{R^2} \right), \quad (33)$$

⁴Note that the value \mathcal{H}_{SS} uses the inferred ratio \mathcal{R}_{26} for the solar system, but assumes an aluminum rich composition (see Hevey & Sanders 2006).

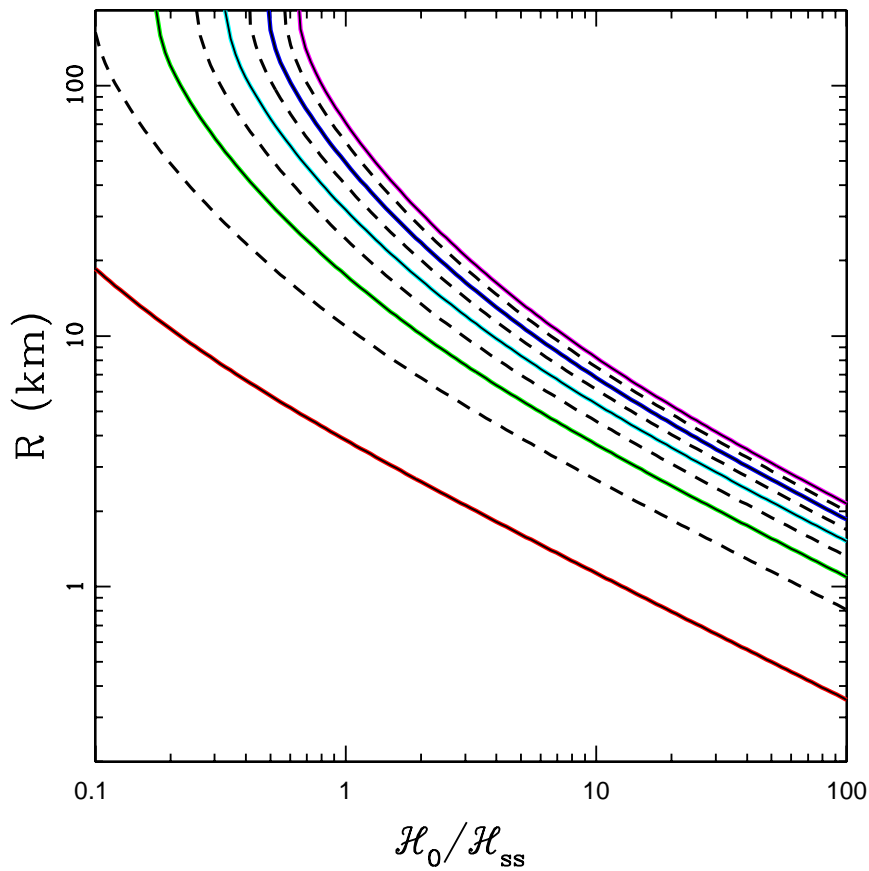


Fig. 4.— Internal temperatures of planetesimals as a function of size R and radioactive heating rate \mathcal{H}_0 . The curves show contours for which the planetesimals reach a given temperature over 90 percent of their radial extent, for $T = 1000$ K (red), 2000 K (green), 3000 K (cyan), 4000 K (blue), and 5000 K (magenta). Dashed curves show $T = \text{constant}$ contours for intermediate values of temperature.

where T_S is the surface temperature and where the temperature scale T_x is determined by the rock properties

$$T_x \equiv \frac{\mathcal{H}R^2}{6K_c} \approx 51 \text{ K} \left(\frac{\mathcal{H}}{\mathcal{H}_{SS}} \right) \left(\frac{R}{1 \text{ km}} \right)^2. \quad (34)$$

In order for most of the planetesimal volume to be molten, the temperature scale T_x must be significantly above the melting temperature of rock. For example, if we require $T > 2000 \text{ K}$ at $r/R = 0.90$, the scale $T_x \sim 5000 \text{ K}$. For solar system heating rates, one thus requires $R \gtrsim 10 \text{ km}$. As the SLR abundances increase, the critical radius for melting scales (approximately) as $R_{crit} \sim \mathcal{H}^{-1/2}$ (consistent with the slope of the curves on the right side of Figure 4).

4.3. Internal Luminosity of Rocky Planets

Once a planet has formed out of the planetesimals, the internal luminosity will be enhanced due to radioactive decay of ^{26}Al (and other SLRs). This luminosity contribution can be written in the form

$$L_{\text{in}} = \lambda \epsilon X_{26} \left(\frac{M_{\text{plan}}}{26m_p} \right) e^{-\lambda t} \approx 1.2 \times 10^{26} \text{ erg s}^{-1} \left(\frac{M_{\text{plan}}}{M_R} \right) e^{-\lambda t}. \quad (35)$$

Here the time variable is measured from the production of the planetesimals, as radioactive enrichment becomes highly inefficient when rocky bodies reach that size. Since the planet, with mass M_{plan} , is made from the rocky material in the reconnection annulus, with mass M_R , we expect the two mass scales to be comparable. As a result, this scenario defines a characteristic planetary luminosity $L \sim 3 \times 10^{-8} L_\odot$, which is independent of the planetary mass (if planet formation is efficient so that $M_{\text{plan}} \sim M_R$).

For comparison, the power intercepted by the planet from its host star takes the form

$$P_* = L_* \left(\frac{R_{\text{plan}}}{2r} \right)^2 \approx 1.8 \times 10^{26} \text{ erg s}^{-1} \left(\frac{R_{\text{plan}}}{R_\oplus} \right)^2 \left(\frac{r}{0.1 \text{ AU}} \right)^{-2}, \quad (36)$$

where we have used $L_* = L_\odot$. For earth-sized planets, the external power is roughly comparable to the internal power for the expected abundances of SLRs. For larger planets, the external power is relatively larger. This ordering only holds for newly formed planets, however, as the internal luminosity decreases exponentially with time. Finally, note that the residual heat left over from planet formation provides another power source for young planets.

5. Conclusion

This paper constructs a model for the production of ^{26}Al , and other SLRs, during the epoch of planet formation. In this scenario, cosmic rays are generated via magnetic reconnection events near the truncation radius that marks the inner edge of the planet-forming disk. The rocky bodies in this region have typical sizes $R \sim 1$ cm, and are exposed to an intense flux of cosmic rays that drive spallation reactions. The enriched pebbles are subsequently incorporated into planetesimals ($R \sim 1 - 100$ km), which eventually become fully formed rocky planets ($R \sim 6000 - 10^4$ km). Our main results are summarized below (Section 5.1) along with a brief discussion of their implications (Section 5.2).

5.1. Summary of Results

The magnetic truncation radius of T Tauri star/disk systems falls in a range centered on $r_X \sim 0.1$ AU. This region is coincident with a substantial population of observed exoplanets found in multi-planet systems (Figure 1).

The planet-forming material in the reconnection region is exposed to intense cosmic ray radiation that will synthesize radioactive nuclei through spallation reactions. The resulting nuclear isotope ratio for ^{26}Al has a fiducial value $\mathcal{R}_{26} \approx 10^{-3}$, a factor of ~ 20 larger than the isotope ratio inferred for our solar system (Figure 3).

The predicted isotope ratio \mathcal{R}_{26} scales inversely with the total amount of rocky material M_R in the reconnection region. If we assume that the planets form from the same reservoir of material, then $\mathcal{R}_{26} \propto M_{\text{plan}}^{-1}$. The cosmic radiation is attenuated by propagating through rocky material, where Coulomb losses provide the dominant source of energy loss. This treatment does not include spallation produced via secondary particles (e.g., Pavlov et al. 2014), so the abundances presented here represent lower limits.

With the enhanced abundances of SLRs, the minimum radius necessary for planetesimals to become completely molten decreases (Figure 4). For the expected isotope ratio corresponding to $M_R = 1M_{\oplus}$, planetesimals are predicted to melt for radii greater than $R \gtrsim 3$ km. For comparison, the radius needed for planetesimals to melt is about ~ 20 km for the standard abundance of radioactive material.

Since the planetesimals are expected to entirely molten, the composition of planets forming near $r \sim 0.1$ AU can be different than those forming farther out. The volatile component of the planet will be determined by those materials that are soluble in magma (see the review of Chao et al. 2020). In particular, water is efficiently out-gassed in molten

planetesimals (e.g., Lichtenberg et al. 2019) so that planets forming in the reconnection region are predicted to be severely dehydrated. These effects should be elucidated in future work.

With the expected enhancement of SLRs, planets with masses $M_{\text{plan}} \sim 1M_{\oplus}$ generate significant internal luminosities due to radioactive decay. If the planets form rapidly, this internal luminosity can be larger than the power intercepted from the host stars (at $r = 0.1$ AU and at early times). As a result, assessments of atmospheric evaporation must include internal energy sources due to radioactivity.

For the most common stars in the galaxy, with masses $M_* \sim 0.25 M_{\odot}$, the reconnection region for cosmic ray exposure ($r_X \sim 0.1$ AU) corresponds to the habitable zone (after the stars reach the main sequence). This paper shows that the raw materials that make up this class of potentially habitable planets are naturally irradiated by local cosmic rays (Figure 1), leading to spallation and radioactive enrichment (Figure 3). One potential consequence of this chain of events is that habitable zone planets orbiting red dwarfs are depleted in water and other volatiles.

5.2. Discussion

For the scenario developed in this paper, the predictions for enhanced levels of radioactive enrichment depend on the timing of planet-forming events. The rocky bodies — in the form of pebbles — must be large enough ($R \gtrsim 1$ cm) that they can reside in the reconnection region and avoid being swept into the star (keep in mind that this region is depleted in gas). At the same time, the rocks must remain small enough ($R \lesssim 300$ cm) so that they can be efficiently irradiated and enriched. The subsequent production of planetesimals must then occur rapidly in order for the radioactive species to remain active and melt the larger rocky bodies. The exposure time t_{exp} of the pebbles must thus be somewhat longer than the half-life $t_{1/2} \sim 0.72$ Myr, whereas the time t_{pls} required to produce planetesimals must be shorter. The required ordering of time scales ($t_{\text{pls}} < t_{1/2} < t_{\text{exp}}$) is typically satisfied in planet formation models that operate via the streaming instability (Drazkowska et al. 2016; Simon et al. 2016; Johansen et al. 2021). However, if departures occur, for example shorter exposure times while the rocky bodies are small, the level of radioactive enrichment would be correspondingly smaller. A related issue is that the gas in the reconnection must be optically thin ($\Sigma \lesssim 0.01$ g cm⁻²) for maximum exposure to cosmic rays, whereas the streaming instability is most efficient for comparable densities of gas and solids (Youdin & Goodman 2005). Since the surface density of solids is larger in this scenario, the growth of planetesimals by streaming instability is correspondingly slower. On the other hand, the solids are already

concentrated and can collapse to form planetesimals via gravitational instability (Goldreich & Ward 1973; Youdin & Shu 2002).

Another possible way to reduce enrichment is for planets to form at more distant radial locations in the disk and then migrate inwards. Since the degree of radioactive heating can be much larger for the case of in situ formation, the composition of planets, and the corresponding the mass-radius relation, could be different for the two scenarios. Future work should thus outline the detailed chemical compositions resulting from melted planetesimals with varying levels of radioactive enrichment. Such studies could then predict how planetary properties are different for planets that migrate versus those that form locally.

In the present treatment, the solution to the diffusion equation for the planetesimal temperature assumes that the body is made of solid rock (so that the thermal diffusivity is constant). The resulting temperature profiles provide a good estimate for when and where the rocky planetesimals become hot enough to melt. After the body is sufficiently molten, however, convection carries the heat through the planetary layers where temperatures are high. Future work should thus construct evolutionary models (building on the work of Hevey & Sanders 2006) for planetesimals where the internal heat is transported convectively. The time dependent temperature structure can then be used to determine the degree of volatile losses and hence the chemical composition of the objects. In addition, the largely molten nature of the planetesimals could affect their subsequent assembly into larger planetary bodies. Collisions between the resulting liquid entities should thus be studied. Once planets are formed, the internal luminosity from SLRs will affect the surface temperatures and the rate of atmospheric mass loss. This process should also be modeled in greater detail.

This paper has focused on the isotope ^{26}Al , which is expected to have the largest impact on planetesimals and forming planets. Other SLRs can be made through spallation and should be included in future work. Consider, for example, the case of ^{53}Mg , with half-life 3.7 Myr. The solar system abundance of this species is a factor of 10 smaller than that of ^{26}Al . If the two isotopes are produced with initial abundance ratios similar to those of our solar system, then the relative power contribution will vary with time according to $L_{\text{Mn}53}/L_{\text{Al}26} = (\lambda_{53}/\lambda_{26}) (X_{26}/X_{53}) \exp[-(\lambda_{26} - \lambda_{53})t] \approx 0.02 \exp[t/1.3\text{Myr}]$. The manganese luminosity should thus dominate after ages of ~ 5 Myr, although by that time the overall power will have decreased by a factor of ~ 100 . In addition to SLRs, long-lived radioactive nuclei can also be produced by spallation. For example, protons of sufficiently high energy (~ 100 MeV) can produce ^{40}K through spallation reactions with iron (mostly ^{56}Fe , which is relatively abundant).

This paper shows that planets forming in close proximity to their host stars are exposed to enormous fluxes of particle radiation and can become substantially enriched in SLRs.

The degree of radioactive enrichment will vary with the planet location, the timing of planet forming events, and the details of the local magnetic field structure. The resulting variations in planet properties — due to heating, differentiation, out-gassing, evaporation, and other processes — will thus add to the diversity found in the observed population of extra-solar planets.

Acknowledgment: We would like to thank Konstantin Batygin, Juliette Becker, George Fuller, Evan Grohs, Alex Howe, and Chris Spalding for useful discussions. We also thank an anonymous referee for comments and suggestions. This work was supported by the Leinweber Center for Theoretical Physics and by the University of Michigan.

REFERENCES

- Adams, F. C. 2020, *ARA&A*, 48, 47
- Batalha, N. M., Borucki, W. J., Bryson, S. T., et al. 2011, *ApJ*, 729, 27
- Blandford, R. D., & Payne, D. G. 1982, *MNRAS*, 199, 883
- Carlslaw, H. S., & Jäger, J. C. 1959, *Conduction of Heat in Solids* (Oxford: Oxford Univ. Press)
- Chao, K.-H., de Graffenried, R., Lach, M., Nelson, W., Truax, K., & Gaidos, E. 2020, [arXiv:2012.07337](https://arxiv.org/abs/2012.07337)
- Clayton, D. D., & Jin, L. 1995, *ApJ*, 451, 681
- Cleeves, L. I., Adams, F. C., Bergin, E. A., & Visser, R. 2013, *ApJ*, 777, 28
- Desch, S. A., Morris, M. A., Connolly, H. C., & Boss, A. P. 2010, *ApJ*, 725, 692
- Drazkowska, J., Alibert, Y., & Moore, B. 2016, *A&A*, 594, 105
- Duprat, J., & Tatischeff, V. 2007, *ApJ*, 671, 69
- Feigelson, E. D., & Montmerle, T. 1999, *ARA&A*, 37, 363
- Feigelson, E. D., Getman, K., Townsley, L., et al. 2005, *ApJS*, 160, 379
- Fisk, L. A. 1978, *ApJ*, 224, 1048
- Fitoussi, C., Duprat, J., Tatischeff, V. et al 2008, *Phys. Rev. C*, 78, 044613

- Formato, V., Adriani, O., Barbarino, G. C. et al. 2014, *Nuc. Instr. Meth. Phys. Res.*, A742, 273
- Garrard, T.L., Stone, E.C, & Vogt, R.E. 1973, in *High Energy Phenomena on the Sun Symposium Proceedings*, ed. I. A. Ibragimov AND G. E. Kocharov, (NASA SP-342), p. 341
- Gounelle, M., Shu, F. H., Shang, H., Glassgold, A. E., Rehm, K. E., & Lee, T. 2001, *ApJ*, 548, 1051
- Grimm, R. E. & McSween, H. Y. 1993, *Science*, 259, 653
- Ghosh, P., & Lamb, F. K. 1978, *ApJ*, 223, L83
- Goldreich, P., & Ward, W. R. 1973, 183, 1051
- Goswami, J. N., Marhas, K. K., & Sahijpal, S. 2001, *ApJ*, 549, 1151
- Gounelle, M., Chaussidon, M., & Rollion-Bard, C. 2013, *ApJ*, 763, 33
- Hevey, P. J., & Sanders, I. S. 2006, *Met. Plan. Sci.*, 41, 95
- Ikoma, M., Elkins-Tanton, L., Hamano, K., & Suckale, J. 2018, *SSRv*, 214, 76
- Jacquet, E. 2019, *A&A*, 624, 131
- Johansen, A., Ronnet, T., Bizzarro, M., Schiller, M., Lambrechts, M., Nordlund, A., & Lammer, H. 2021, *Science Advances*, 17, 0444
- Johns-Krull, C. M. 2007, *ApJ*, 664, 975
- Jura, M., Xu, S., & Young, E. D. 2013, *ApJ*, 775, L41
- Koning, A. J., Rochman, D., Sublet, J., Dzysiuk, N., Fleming, M., & van der Marck, S. 2019, *Nuclear Data Sheets*, 155, 1
- LaTourrette, T., & Wasserburg, G.J. 1998, *EPSL*, 159, 91
- Lee, T., Papanastassiou, D. A., & Wasserburg, G. J. 1977, *ApJ*, 211, 107L,
- Lee, T., Shu, F. H., Shang, H., Glassgold, A. E., & Rehm, K. E. 1998, *ApJ*, 506, 898
- Leya, I., Halliday, A. N., & Wieler, R. 2003, *ApJ*, 594, 605
- Lichtenberg, T., Golabek, G. J., Burn, R., et al. 2019, *Nature Astronomy*, 3, 307

- Liu, M.-C., & McKeegan, K. D. 2009, *ApJ*, 697, 145
- Lodders, K. 2003, *ApJ*, 591, 1220
- Mewaldt, R. A., Looper, M. D., Cohen, C.M.S., Haggerty, D. K., Labrador, A. W., Leske, R. A., Mason, G. M., Mazur, J. E., & von Rosenvinge, T. T. 2012, *Space Sci. Rev.*, 171, 97
- Moskovitz, N., & Gaidos, E. 2011, *M&PS*, 46, 903
- Najita, J. R., & Shu, F. H. 1994, *ApJ*, 429, 808
- Padovani, M., Marcowith, A., Hennebelle, P., & Ferrière, K. 2016, *A&A*, 590, 8
- Pavlov, A. A., Pavlov, A. K., Ostryakov, V. M., Vasilyev, G. I., Mahaffy, P., & Steele, A. 2014, *J. Geophys. Res.*, 119, 1390
- Preibisch, T., Kim, Y.-C., Favata, F., et al. 2005, *ApJS*, 160, 401
- Reames, D. V., Barbier, L. M., Von Rosenvinge, T. T., Mason, G. M., Mazur, J. E., & Dwyer, J. R. 1997, *ApJ*, 483, 515
- Reames, D. V. 1999, *Space Sci. Rev.*, 90, 413
- Reames, D. V. 2013, *Space Sci. Rev.*, 175, 53
- Reedy, R. C., & Marti, K. 1991, in *The Sun in Time*, ed. C. P. Sonett, M. S. Giampapa, & M. S. Matthews (Tucson : Univ. Arizona Press), 260
- Reedy, R. C., 2015, *Nucl. Instr. Meth. Phys. Res. B*, 361, 500
- Reiter, M. 2020, *A&A*, 644, 1
- Schramm, D. N. 1971, *Ap&SS*, 13, 249
- Shu, F. H., Shang, H. & Lee, T. 1996, *Science*, 271, 1545
- Shu, F. H., Shang, H., Glassgold, A. E., & Lee, T. 1997, *Science*, 277, 1475
- Shu, F. H., Shang, S., Gounelle, M., Glassgold, A. E. & Lee, T. 2001, *ApJ*, 548, 1029
- Simon, J. B., Armitage, P. J., Li, R., & Youdin, A. N. 2016, 822, 55
- Soppera, N., Dupont, E., & Fleming, M. 2020, *JANIS Book of Proton Induced Cross Sections*, OECD NEA Data Bank

- Soppera, N., Dupont, E., & Fleming, M. 2020 JANIS Book of Alpha Induced Cross Sections, OECD NEA Data Bank
- Soppera, N., Dupont, E., & Fleming, M. 2020 JANIS Book of Helion Induced Cross Sections, OECD NEA Data Bank
- Sossi, P. A., Moynier, F., Chaussidon, M., Villeneuve, J., Kato, C., & Gounelle, M. 2017, *Nature Astronomy*, 1, 55
- Urey, H. C. 1955, *PNAS*, 41, 127
- Van Hollebeke, M.A.I., Ma Sung, L. S., & McDonald F. B. 1975, *Solar Phys.* 41, 189
- Wasserburg, G. J. 1985, in *Protostars and Planets II*, ed. D. C. Black & M. S. Matthews (Tucson: Univ. Arizona Press), 703
- Youdin, A. N., & Goodman, J. 2005, *ApJ*, 620, 459
- Youdin, A. N., & Shu, F. H. 2002, *ApJ*, 580, 1